Nano Research

Open Access

Research Article

Defect and heterogeneous interface engineering of NRGO/$MgFe_2O_4$@NC composite aerogels for high-efficiency electromagnetic wave absorption, radar stealth and thermal insulation

Ruiwen Shu[1] ✉, Youran Zhang[1], Kunlong Yun[1], Yongmei Li[1], Xiaoqing Zhao[2], Bin Wang[2], Konghu Tian[3], Xiaoli Ji[1], and Zhijian Yan[4]

[1] State Key Laboratory for Safe Mining of Deep Coal Resources and Environment Protection, School of Chemical and Blasting Engineering, Anhui University of Science and Technology, Huainan 232001, China
[2] School of Materials Science and Engineering, Anhui University of Science and Technology, Huainan 232001, China
[3] Analytical and Testing Center, Anhui University of Science and Technology, Huainan 232001, China
[4] Chengdu Tory Thalez Electronic Application Technology Co., Ltd., Chengdu 610036, China

Cite this article: *Nano Research*, **2026**, *19*, 94908344. https://doi.org/10.26599/NR.2026.94908344

ABSTRACT: Reduced graphene oxide (RGO) has been widely applied in the field of electromagnetic wave (EMW) absorption. However, its excessively high conductivity results in poor impedance matching, causing the incident waves to undergo intense reflection and weak absorption. In this work, nitrogen-doped reduced graphene oxide/magnesium ferrite@nitrogen-doped carbon (NRGO/$MgFe_2O_4$@NC) composite aerogels were prepared by solvothermal synthesis, *in-situ* polymerization, annealing treatment, and hydrothermal self-assembly processes. Significantly, the ternary composite aerogels exhibited the ultralow bulk density and a unique three-dimensional (3D) porous network structure. Furthermore, the $MgFe_2O_4$ microspheres were uniformly coated with the NC layer, and a special chain-like core–shell structure was observed, which could form abundant heterogeneous interfaces. It was notable that when the addition amount of $MgFe_2O_4$@NC was 30 mg and the filling ratio was 6 wt.%, the minimum reflection loss was −59.79 dB at a matching thickness of 3.3 mm, and the maximum effective absorption bandwidth reached 7.2 GHz at a thickness of 2.83 mm. The synergistic effect of multiple reflections, conduction loss, polarization loss, and eddy current loss, as well as the optimized impedance matching, significantly enhanced the EMW absorption performance. The research results of radar cross section (RCS) simulation demonstrated that the NRGO/$MgFe_2O_4$@NC composite aerogel had excellent radar stealth performance. Additionally, the prepared ternary composite aerogels exhibited good thermal insulation property. Therefore, the prepared ternary composite aerogels could be used as lightweight and multifunctional EMW absorbers.

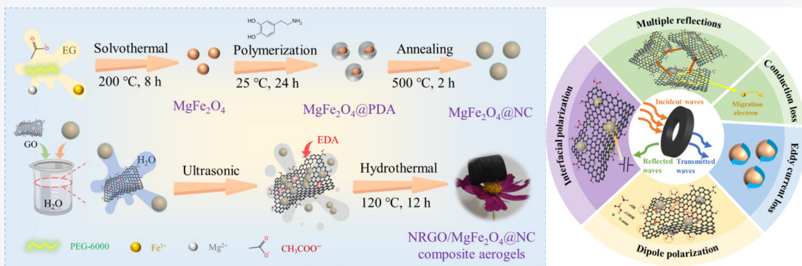

KEYWORDS: electromagnetic wave absorption, defect engineering, core–shell structure, nitrogen-doped graphene, aerogel

1 Introduction

In the present era, electromagnetic waves (EMWs) have been widely applied in military, communication, and satellite navigation fields, bringing great convenience to humanity [1, 2]. However, this phenomenon also brings many problems, such as electromagnetic interference and electromagnetic pollution, which may have certain adverse effects on the normal operation of instruments and human health [1, 2]. Therefore, the development of new EMW absorbing materials has become an extremely important research hotspot. The current research mainly focuses on developing EMW absorbers with lightweight, strong absorption intensity, and wide effective absorption bandwidth (EAB) [3]. However, in the face of the increasingly complex electromagnetic environment and the urgent need for weapon system stealth, the development of multifunctional EMW absorbers with integrated excellent wave absorption, radar

Received: October 30, 2025; **Revised:** December 11, 2025
Accepted: December 14, 2025

✉Address correspondence to rwshu@aust.edu.cn

stealth, and thermal insulation properties holds significant importance [4, 5]. Especially, the excellent thermal insulation properties safeguard electronic devices against extreme temperatures.

Spinel magnesium ferrite ($MgFe_2O_4$) is widely used as a magnetic EMW absorbing material due to its low synthesis cost, high permeability, and strong chemical stability [6, 7]. However, the high density, narrow absorption bandwidth, and large matching thickness limit its practical application. As a typical carbon nanomaterial, graphene has attracted much attention in the field of EMW absorption due to its special two-dimensional (2D) structure, excellent electrical conductivity, low density, and large specific surface area [8, 9]. However, its excessive electrical conductivity may lead to imbalance in electromagnetic parameters, thereby causing impedance mismatch between the absorber and free space. As a result, the incident waves will be reflected at the material interface. To solve this problem, a common strategy is to adjust the electromagnetic parameters of the absorber through magnetic compositing or structural engineering, thereby improving the wave absorption performance of graphene-based composites [8, 9].

Reduced graphene oxide (RGO) is usually obtained through the oxidation and reduction of graphene. It contains abundant structural defects and residual oxygen-containing functional groups [9, 10]. These inherent characteristics enable RGO to more effectively absorb and dissipate electromagnetic energy, and thus it has received extensive attention [9, 10]. In recent years, RGO aerogels with a three-dimensional (3D) porous network structure, extremely low density, and superior thermal insulation properties have shown great potential as lightweight and multifunctional EMW absorbing materials [9, 11, 12]. However, a single dielectric loss mechanism results in the poor wave attenuation capability of pure RGO aerogels.

Previous studies have shown that the wave absorption capability of RGO aerogels can be enhanced by combining with dielectric or magnetic components [13–23], or by doping with heteroatoms [24–27]. For instance, Hou et al. prepared RGO/MoS_2 composite aerogels by a two-step hydrothermal method. It was noteworthy that when the filling ratio (φ_w) was 40 wt.%, the minimum reflection loss (RL_{min}) reached −45.79 dB, and EAB was 6.56 GHz [17]. Wang et al. developed CoNi/RGO composite aerogels through solvothermal synthesis and subsequent carbonization process. Significantly, with only a low φ_w of 7 wt.%, the RL_{min} reached −53.3 dB, and EAB was 4.8 GHz [19]. Ren et al. constructed $ZnFe_2O_4$/RGO composite aerogels through hydrothermal reduction treatment. Specifically, the RL_{min} of the obtained composite aerogel was −29.12 dB, and EAB reached 3.57 GHz [21]. Unfortunately, the preparation of 3D RGO-based magnetic/dielectric composites with comprehensively excellent EMW absorption properties remains a major challenge. To the best of our knowledge, there are relatively few studies currently focusing on the construction of 3D ternary composite aerogels by integrating the advantages of lightweight RGO aerogels, magnetic $MgFe_2O_4$ microspheres, and conductive nitrogen-doped carbon (NC).

In this study, nitrogen-doped reduced graphene oxide/magnesium ferrite@nitrogen-doped carbon (NRGO/$MgFe_2O_4$@NC) composite aerogels were prepared by the solvothermal synthesis, *in-situ* polymerization, annealing treatment, and hydrothermal self-assembly processes. The crystal structure, degree of graphitization, composition, morphology, static magnetic properties, and electromagnetic parameters of NRGO/$MgFe_2O_4$@NC composite aerogels were characterized by various analytical techniques. The influence of addition amount of $MgFe_2O_4$@NC on the electromagnetic parameters and EMW absorption properties of the ternary composite aerogels was investigated. It was worth noting that the unique 3D porous network structure and chain-like core–shell structure of the composite aerogels not only generated rich heterogeneous interfaces to promote interfacial polarization, but also optimized impedance matching, thereby improving the dissipation capability of electromagnetic energy. The potential EMW absorption mechanism of NRGO/$MgFe_2O_4$@NC composite aerogels was also elucidated. Additionally, the obtained NRGO/$MgFe_2O_4$@NC composite aerogels exhibited excellent radar stealth and thermal insulation properties.

2 Experimental section

2.1 Synthesis of $MgFe_2O_4$@NC microspheres

The synthesis method of $MgFe_2O_4$ microspheres was the same as the method used in our previous studies [7, 28]. $MgFe_2O_4$@polydopamine (PDA) microspheres were synthesized by an *in-situ* polymerization reaction. Firstly, 0.12 g of trihydroxymethyl aminomethane (Tris) was dissolved in 100 mL of deionized water, and 0.1 g of $MgFe_2O_4$ was dispersed in the above Tris buffer solution through ultrasonic treatment for 0.5 h. Then, 0.12 g of hydroxy-1,2-diaminopropane (DA) was added. After 24 h of mechanical stirring, the obtained product was washed several times with deionized water and subsequently freeze-dried for 48 h to produce $MgFe_2O_4$@PDA microspheres. Finally, $MgFe_2O_4$@PDA microspheres were annealed at 500 °C for 2 h in an Ar atmosphere and transformed into $MgFe_2O_4$@NC microspheres.

2.2 Preparation of NRGO/$MgFe_2O_4$@NC composite aerogels

NRGO/$MgFe_2O_4$@NC composite aerogels were prepared by the hydrothermal self-assembly method. Firstly, 90 mg of graphene oxide (GO) was added to 30 mL of deionized water. After ultrasonic treatment for 1 h, a uniform GO suspension (3 $mg \cdot mL^{-1}$) was obtained. Then, a certain amount of $MgFe_2O_4$@NC microspheres were added to the above GO suspension. The mixture was ultrasonicated for 0.5 h, then mechanically stirred for 0.5 h. Afterwards, 180 μL of ethylenediamine (EDA) was added dropwise, stirred for another 2 h, and then transferred to a Teflon-lined stainless-steel autoclave, where it was reacted at 120 °C for 12 h. Finally, the obtained hydrogels were dialyzed in 10% (v/v) C_2H_5OH/H_2O solution for 36 h and then freeze-dried at −50 °C for 48 h, thereby forming the NRGO/$MgFe_2O_4$@NC composite aerogels. For convenience, the NRGO/$MgFe_2O_4$@NC composite aerogels prepared with different addition amounts of $MgFe_2O_4$@NC were labeled as S1 (15 mg), S2 (30 mg), and S3 (45 mg), respectively.

Figure 1 shows the schematic diagram of the preparation process of NRGO/$MgFe_2O_4$@NC composite aerogels. Firstly, $MgFe_2O_4$ microspheres were synthesized through a simple solvothermal reaction. Then, by adding DA to the weakly alkaline $MgFe_2O_4$ suspension, the *in-situ* polymerization reaction of DA on the surface of $MgFe_2O_4$ was completed. As a result, a layer of PDA shell was uniformly covered on the surface of $MgFe_2O_4$. Afterwards, the $MgFe_2O_4$@PDA microspheres were annealed in an Ar atmosphere

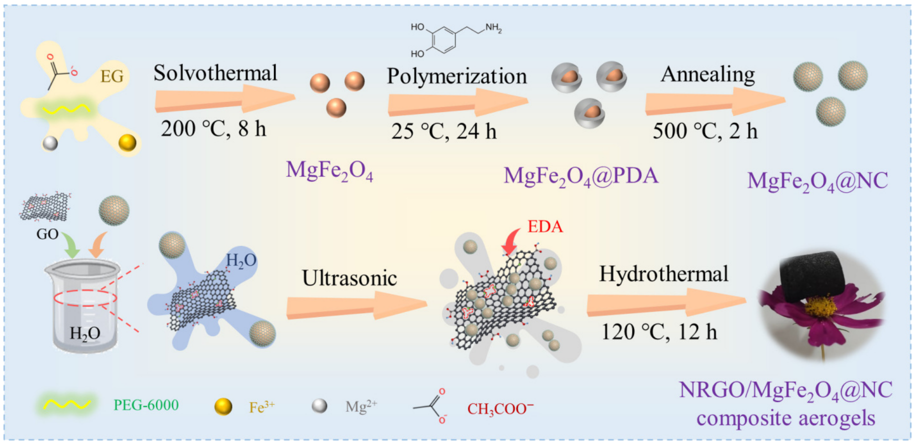

Figure 1 Schematic diagram of the preparation process of NRGO/$MgFe_2O_4$@NC composite aerogels.

to form $MgFe_2O_4$@NC microspheres. Finally, the NRGO/$MgFe_2O_4$@NC ternary composite aerogels were prepared through a hydrothermal reaction, during which nitrogen atoms were simultaneously doped into the crystal lattice of RGO.

3 Results and discussion

3.1 Structure and composition analysis

The crystal structure of NRGO/$MgFe_2O_4$@NC composite aerogels was characterized by X-ray diffraction (XRD). As shown in Fig. 2(a), the diffraction peaks at 2θ = 18.3°, 30.2°, 35.6°, 43.3°, 53.7°, 57.2°, and 62.8° correspond to the (111), (220), (311), (400), (422), (511), and (440) crystal planes of $MgFe_2O_4$ (JCPDS No. 73-1960), respectively [7, 28]. The hump peak at 24.1° can be assigned to the (002) crystal plane of RGO [28]. It is worth noting that as the addition amount of $MgFe_2O_4$@NC increases, the diffraction peak of RGO gradually weakens.

Thermal gravimetric analysis (TGA) test was conducted for determining the contents of $MgFe_2O_4$ in the obtained ternary composite aerogels. From Fig. 2(b), it can be seen that within the temperature range below 220 °C, the weight loss of S1–S3 is extremely small. This may be because only the chemical groups on NRGO are removed. Within the temperature range of 220 to 530 °C, the weight of S1–S3 decreases significantly, mainly due to the decomposition of NRGO and NC [29]. When the temperature exceeds 530 °C, a stable weight plateau is reached. Therefore, the residual product should be $MgFe_2O_4$. The weight percentages of $MgFe_2O_4$ in S1–S3 are approximately 11.9 wt.%, 31.4 wt.%, and 48.8 wt.%, respectively.

Raman spectroscopy was widely used to analyze the degree of graphitization of carbonaceous materials. As shown in Fig. 2(c), two Raman scattering peaks are observed at 1596 and 1342 cm^{-1}, representing the G band and D band, respectively [30, 31]. The intensity ratio of D band to G band (I_D/I_G) values of S1–S3 are 1.05, 1.02, and 1.01, respectively. Therefore, with the increase in the addition amount of $MgFe_2O_4$@NC, the degree of graphitization of the composite aerogels shows an upward trend.

The surface chemical composition and elemental valence states of S2 were analyzed by X-ray photoelectron spectroscopy (XPS). The total spectrum (Fig. 2(d)) reveals that S2 contains Mg, Fe, O, N, and C elements. As illustrated in Fig. 2(e), the C 1s spectrum is divided into three peaks, located at 288.6, 285.7, and 284.8 eV, corresponding to C–O, C–N, and C=C/C–C bonds, respectively [24, 28]. The N 1s spectrum is shown in Fig. 2(f), where the binding energies of 398.7, 400, and 401.7 eV correspond to pyridinic-type N, pyrrolic-type N and graphitic-type N, respectively [24, 28]. Figure 2(g) shows the O 1s spectrum. The binding energies at 530.3, 531.8, and 533.4 eV correspond to C–O/C=O, O–H, and metal–O bonds, respectively [28]. Figure 2(h) displays Fe 2p spectrum. The peaks are divided into two types: Fe $2p_{1/2}$ (726.4 and 732.0 eV) and Fe $2p_{3/2}$ (710.7 and 719.3 eV) [7, 28]. The Mg 1s spectrum is shown in Fig. 2(i), where the characteristic peak of Mg^{2+} is observed at 1304.4 eV [7, 28].

3.2 Morphological analysis

Scanning electron microscopy (SEM) and transmission electron microscopy (TEM) were used to characterize the microscopic morphology of NRGO/$MgFe_2O_4$@NC composite aerogels. As depicted in Figs. 3(a) and 3(c)–3(e), all samples display a special 3D porous network structure (indicated by the green dashed circles), which is formed through the self-assembly of adjacent NRGO flakes. It is worth noting that the $MgFe_2O_4$@NC microspheres are uniformly dispersed on the surface of NRGO, and the content of $MgFe_2O_4$@NC microspheres on the surface of NRGO increases with the increase of the addition amount of $MgFe_2O_4$@NC (Figs. 3(b), 3(d), and 3(f)). Furthermore, according to the particle size analysis (Figs. S2–S4 in the Electronic Supplementary Material (ESM)), the average particle sizes of $MgFe_2O_4$, $MgFe_2O_4$@PDA, and $MgFe_2O_4$@NC are 557.3, 675.7, and 655.3 nm, respectively. As shown in Fig. 3(g), it can be confirmed by TEM that $MgFe_2O_4$ is encapsulated by the NC layer, and the thickness of the NC shell is 85 nm. Additionally, the $MgFe_2O_4$@NC microspheres with a unique short chain-like structure are almost uniformly distributed on the wrinkled surface of the NRGO flakes. The high-resolution TEM (HRTEM) image shows that the interplanar spacings of 0.340 and 0.245 nm correspond exactly to the (002) crystal plane of graphite carbon and the (311) crystal plane of $MgFe_2O_4$, respectively [7, 28] (Fig. 3(h)). It can be clearly seen from Fig. 3(i) that the NC shell layer presents a darker color, while the $MgFe_2O_4$ microspheres are brighter in color. Figures 3(j)–3(n) show the energy dispersive X-ray spectroscopy (EDS) mapping images of S2. Significantly, the distribution of C and N elements is uniform, indicating that nitrogen atoms have been doped into RGO. In addition, the O, Fe, and Mg elements are mainly concentrated in the $MgFe_2O_4$ microspheres. Based on the results of structural and morphological analysis, it can be concluded that the

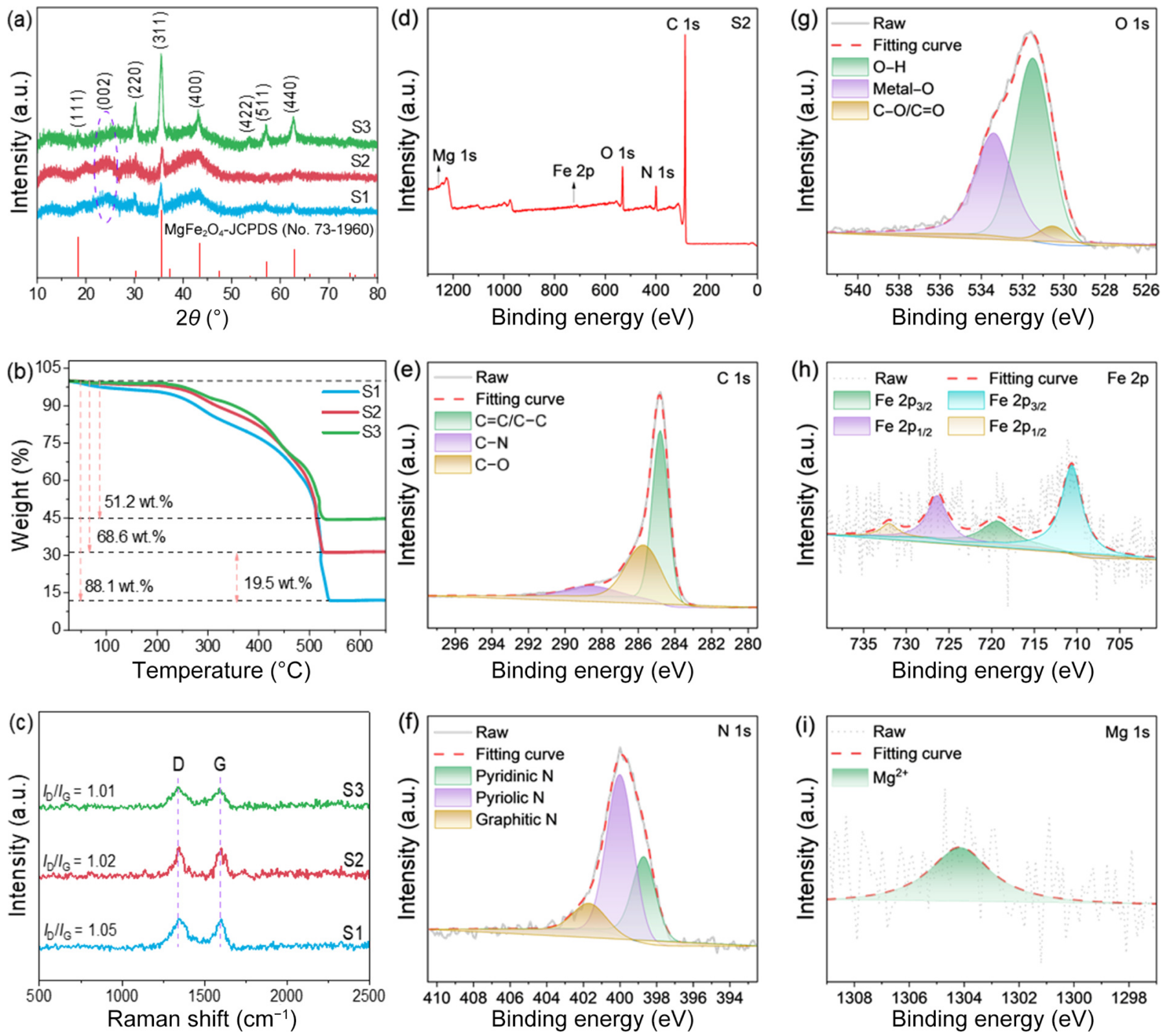

Figure 2 (a) XRD patterns, (b) TGA curves, and (c) Raman spectra of S1–S3. XPS spectra of S2: (d) total spectrum, (e) C 1s, (f) N 1s, (g) O 1s, (h) Fe 2p, and (i) Mg 1s.

NRGO/$MgFe_2O_4$@NC composite aerogels have been successfully prepared.

3.3 EMW absorption properties

RL_{min} and EAB are often used to evaluate the EMW absorption capacity of absorbers. Recent studies have shown that the φ_w has a significant impact on the EMW absorption properties of absorbers [25, 28, 32]. Therefore, the EMW absorption properties of S2 under different filling ratios were studied, as shown in Fig. S5 in the ESM. Specifically, the RL_{min} values of S2 are −4.64, −10.95, −13.18, −17.29, −36.86, −59.79, −42.52, −27.16, and −23.49 dB for 1 wt.%, 2 wt.%, 3 wt.%, 4 wt.%, 5 wt.%, 6 wt.%, 7 wt.%, 8 wt.%, and 9 wt.%, respectively. Meanwhile, the EAB values of S2 are 0, 0, 3.12, 5.36, 6.8, 7.2, 6.56, 8.16, and 7.68 GHz for 1 wt.%, 2 wt.%, 3 wt.%, 4 wt.%, 5 wt.%, 6 wt.%, 7 wt.%, 8 wt.%, and 9 wt.%, separately. Taking into account both the RL_{min} and EAB indicators, the optimal φ_w of 6 wt.% is determined.

The EMW absorption properties of NRGO/$MgFe_2O_4$@NC composite aerogels under a φ_w of 6 wt.% were investigated. The 3D plots of RL and corresponding contour maps for S1–S3 are presented in Figs. 4(a)–4(f). As shown in Figs. 4(a) and 4(d), S1 has the RL_{min} of −21.58 dB at a matching thickness (d) of 2.5 mm and the maximum EAB of 7.12 GHz at d of 3 mm. From Figs. 4(b) and 4(e), it can be seen that S2 shows the optimal RL_{min} of −59.79 dB at d of 3.3 mm, and its widest EAB is 7.2 GHz, corresponding to d of 2.83 mm. As shown in Figs. 4(c) and 4(f), the RL_{min} of S3 reaches −15.56 dB at a thickness d of 5.5 mm, and its EAB is only 4.88 GHz at d of 3.5 mm. It can be clearly seen from Fig. 4(g) that S2 exhibits the best EMW absorption performance with the lowest RL_{min} and the widest EAB. The EAB values of S2 at different matching thicknesses are described in Fig. 4(h). Significantly, the maximum EAB value of S2 reaches up to 7.2 GHz at d of 2.83 mm. To better understand the EMW absorption performance in this study and compare it with recent similar graphene-based composite aerogels reported in Refs. [13, 17, 19, 20, 22, 23, 28, 29], the radar maps of EMW absorption performance of S2 were plotted based on five parameters (RL_{min}, EAB_{max}, d_{RL}, d_{EAB}, and φ_w). Generally, advanced EMW absorbers should meet the following requirements: small φ_w, thin d, low RL_{min}, and broad EAB_{max}. The smaller the area enclosed by the boundary line in the radar maps, the better the comprehensive EMW absorption capacity. The result shows that the area of S2 is the smallest, indicating that S2 has comprehensive excellent EMW absorption performance.

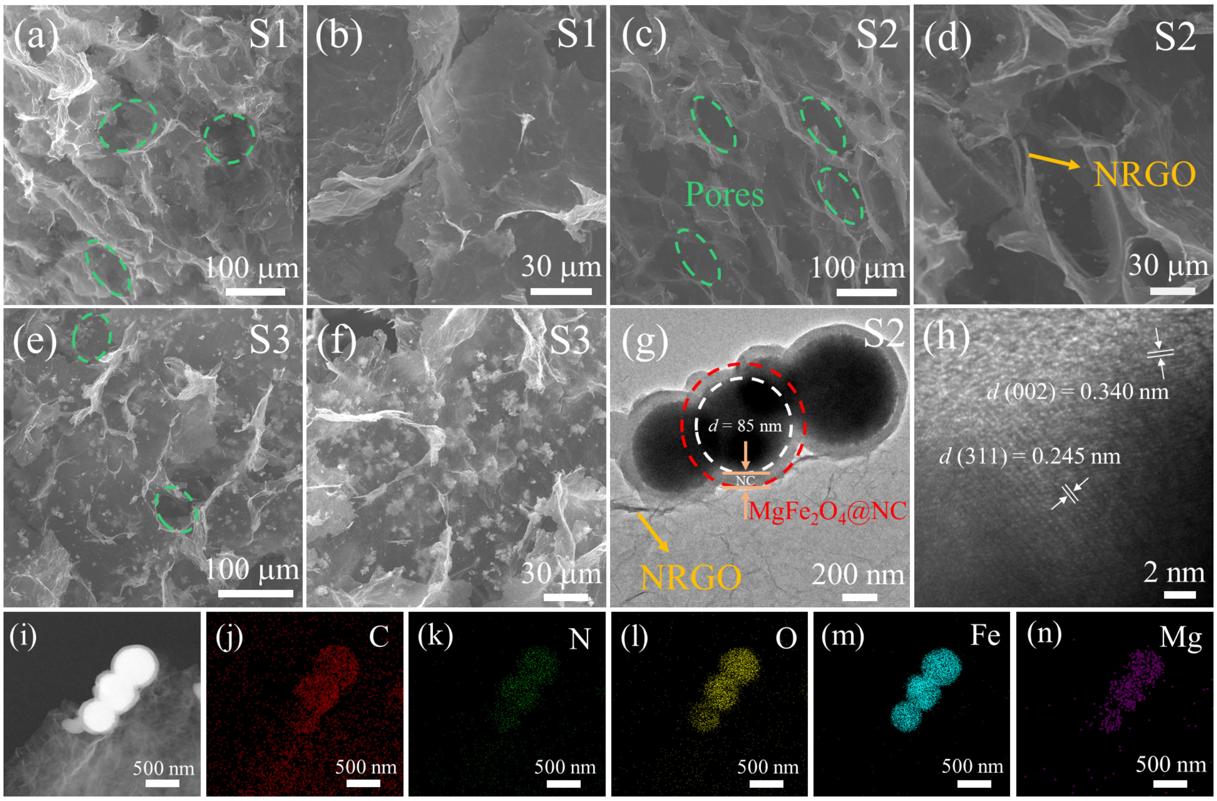

Figure 3 SEM images at different magnifications: (a) and (b) S1, (c) and (d) S2, and (e) and (f) S3. (g) TEM image and (h) HRTEM image. (i) Dark field image and EDS mapping images of (j) C, (k) N, (l) O, (m) Fe, and (n) Mg of S2.

In general, the EMW absorption performance of an absorber depends mainly on its electromagnetic parameters, i.e., relative complex permittivity and complex permeability [33]. The real parts of complex permittivity (ε') and complex permeability (μ') represent the storage capacity of electric field and magnetic field energy, respectively, while the imaginary parts of complex permittivity (ε'') and complex permeability (μ'') denote the dissipation capacity of electric field and magnetic field energy, respectively [34, 35]. Figures 5(a) and 5(b) show the frequency dependence of the complex permittivity of S1–S3. It can be seen that both ε' and ε'' decrease as the frequency increases. This phenomenon is commonly referred to as the frequency dispersion effect, which is helpful for attenuating the electromagnetic energy [36]. In addition, both ε' and ε'' decrease with the increase of the addition amounts of $MgFe_2O_4$@NC. In order to evaluate the dielectric loss capacity, the ratios of ε'' to ε' ($\tan\delta_e$) versus f curves are plotted (Fig. 5(c)). The $\tan\delta_e$ values of S1 are larger than those of S2 and S3, indicating that S1 has the strongest dielectric loss capacity.

The attenuation constant (α) is widely used to assess the electromagnetic dissipation capacity of the absorber, which can be calculated by the following equation [28, 36]

$$\alpha = \frac{\sqrt{2}\pi f}{c} \times \sqrt{(\mu''\varepsilon'' - \mu'\varepsilon') + \sqrt{(\mu''\varepsilon'' - \mu'\varepsilon')^2 + (\varepsilon'\mu'' + \varepsilon''\mu')^2}} \tag{1}$$

The α–f curves of S1–S3 are illustrated in Fig. 5(d). The larger the α value is, the stronger the attenuation loss capacity of the absorber will be. Obviously, the α values decrease in the order of S1 > S2 > S3, manifesting the strongest attenuation loss capacity of S1. However, S1 does not show the best EMW absorption performance. Therefore, when designing high-performance EMW absorbers, the impedance matching characteristic must be taken into account.

In order to analyze the Debye relaxation process, the Cole–Cole curves are plotted according to Eq. (2) [37, 38]

$$\left(\varepsilon' - \frac{\varepsilon_s + \varepsilon_\infty}{2}\right)^2 + (\varepsilon'')^2 = \left(\frac{\varepsilon_s - \varepsilon_\infty}{2}\right)^2 \tag{2}$$

where ε_s represents the static permittivity and ε_∞ stands for the permittivity at high-frequency limit. In general, one semicircle denotes a Debye relaxation process, while the straight-line part at the tail of the Cole–Cole curve signifies the contribution of conduction loss [37, 38]. As shown in Fig. 5(e), it can be observed that there is one and two semicircles in S2 and S3, respectively. As a result, both Debye relaxation and conduction loss are responsible for dielectric loss in both S2 and S3. However, no semi-circle can be identified in S1, indicating that it only has a conduction loss mechanism. The electrical conductivity (σ) was measured by a four-probe meter in this study. From Fig. 5(f), the σ values decrease in the order of S1 > S2 > S3. Therefore, as the addition amount of $MgFe_2O_4$@NC increases, the electrical conductivity shows a downward trend.

The dielectric loss of the absorber includes conduction loss (ε_c'') and polarization loss (ε_p''), which can be simulated by connecting resistors and capacitors in series and parallel circuits [39, 40]. ε_c'' and ε_p'' can be calculated by the following equation [39, 40]

$$\varepsilon'' = \varepsilon_p'' + \varepsilon_c'' = \frac{2\pi f\tau(\varepsilon_s - \varepsilon_\infty)}{1 + (2\pi f)^2\tau^2} + \frac{\sigma}{2\pi f\varepsilon_0} \tag{3}$$

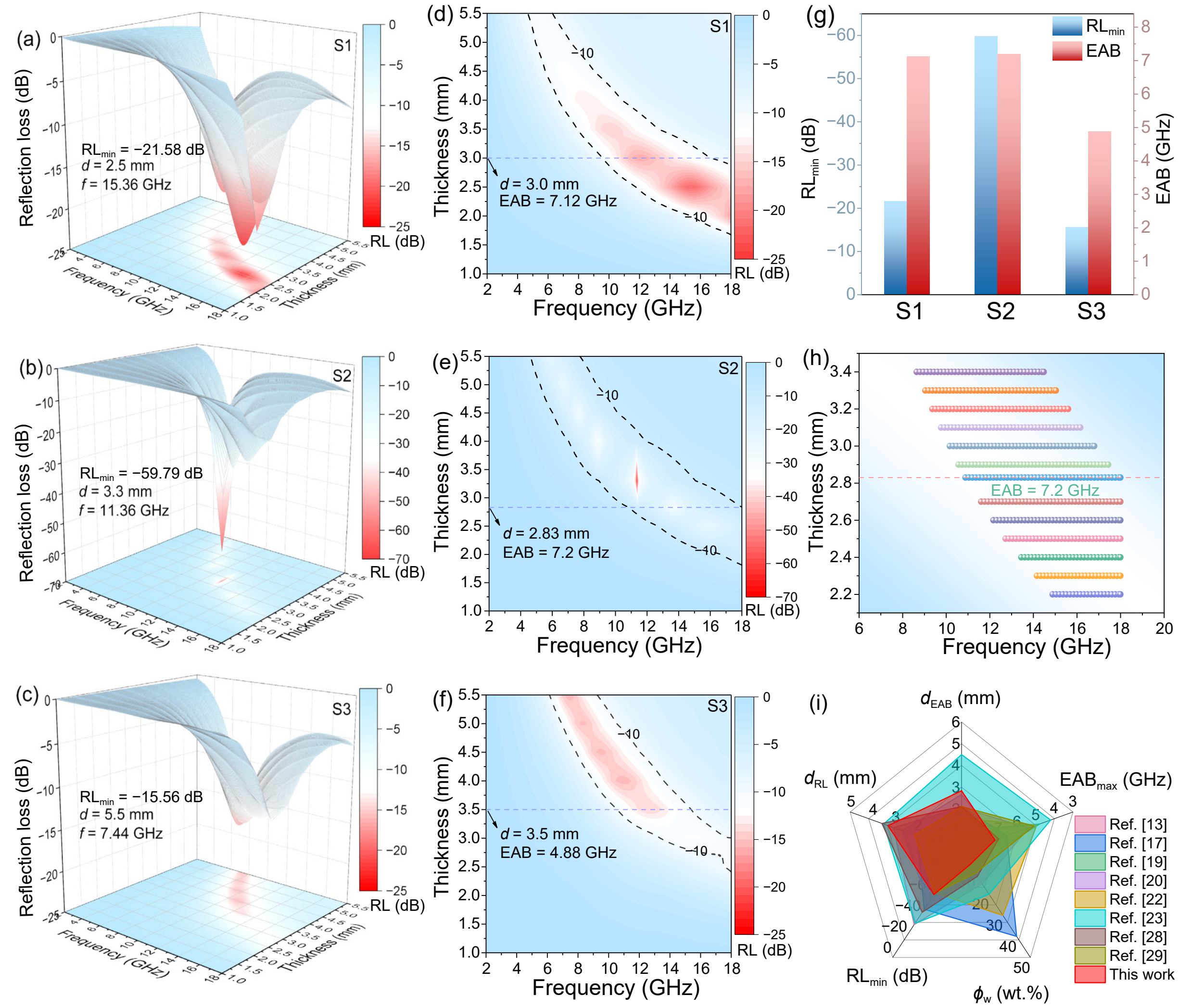

Figure 4 3D plots of RL and 2D counter maps at a filling ratio of 6 wt.%: (a) and (d) S1, (b) and (e) S2, and (c) and (f) S3. (g) Histograms of RL_{min} and EAB of S1–S3. (h) EAB of S2 in the thickness range of 2.2–3.4 mm. (i) Comparing radar maps of EMW absorption performance of S2 with that of other similar composite aerogels.

where τ represents the polarization relaxation time and ε_0 (8.85 × 10^{-12} F·m^{-2}) denotes the vacuum permittivity. As shown in Figs. 5(g) and 5(h), within the range of 2–18 GHz, for both S2 and S3, the values of ε_p'' are greater than ε_c'', thus the polarization loss is the main cause of dielectric loss. However, the dielectric loss of S1 in the high-frequency and low-frequency regions may be attributed to polarization loss and conduction loss, respectively.

Figures 6(a) and 6(b) show the frequency dependance of μ' and μ'' for S1–S3. Specifically, the value of μ' fluctuates around 1, while the value of μ'' varies within the range of 0 to 0.3. Figure 6(c) depicts the magnetic loss tangent ($\tan\delta_m$) versus frequency curves. It is worth noting that the variation trend of $\tan\delta_m$ with frequency is the same as that of μ''. The static magnetic properties of the samples were measured by a vibrating sample magnetometer (VSM) at room temperature. Figure 6(d) displays the hysteresis loops of S1–S3. Notably, all the samples exhibit a typical ferromagnetic behavior [32, 41]. The saturation magnetization (M_s) values of S1–S3 are 7.45, 10.5, and 13.98 emu·g^{-1}, respectively. Meanwhile, the coercive force (H_c) values of S1–S3 are 70.6, 41.73, and 57.62 Oe, separately. As shown in Fig. 6(e), the M_s gradually increases, while the H_c firstly decreases and then increases as the addition amount of $MgFe_2O_4$@NC increases.

The initial magnetic permeability (μ_i) of an absorber is related to a variety of parameters including magnetic anisotropy, M_s, and H_c. The relationship between M_s, H_c, and μ_i is shown in Eq. (4) [42]

$$\mu_i = \frac{M_s^2}{akH_cM_s + b\lambda\xi} \tag{4}$$

Herein a and b are the constants that rely on the material, while the magnetostriction coefficient, proportionality constant, and internal strain are denoted by λ, k, and ξ, respectively. According to the above equation, it can be inferred that a larger M_s and a lower H_c are beneficial to increasing μ_i. Therefore, the magnetic loss capacity of NRGO/$MgFe_2O_4$@NC composite aerogels can be improved by regulating the addition amount of $MgFe_2O_4$@NC.

Generally, the exchange resonance, nature resonance, and eddy current loss are often responsible for magnetic loss in the GHz region. The eddy current coefficient (C_0) can be calculated by Eqs. (5) and (6) [43, 44]

$$\mu'' \approx 2\pi\mu_0(\mu')^2\sigma d^2 f/3 \tag{5}$$

$$C_0 = \mu''(\mu')^{-2}f^{-1} \tag{6}$$

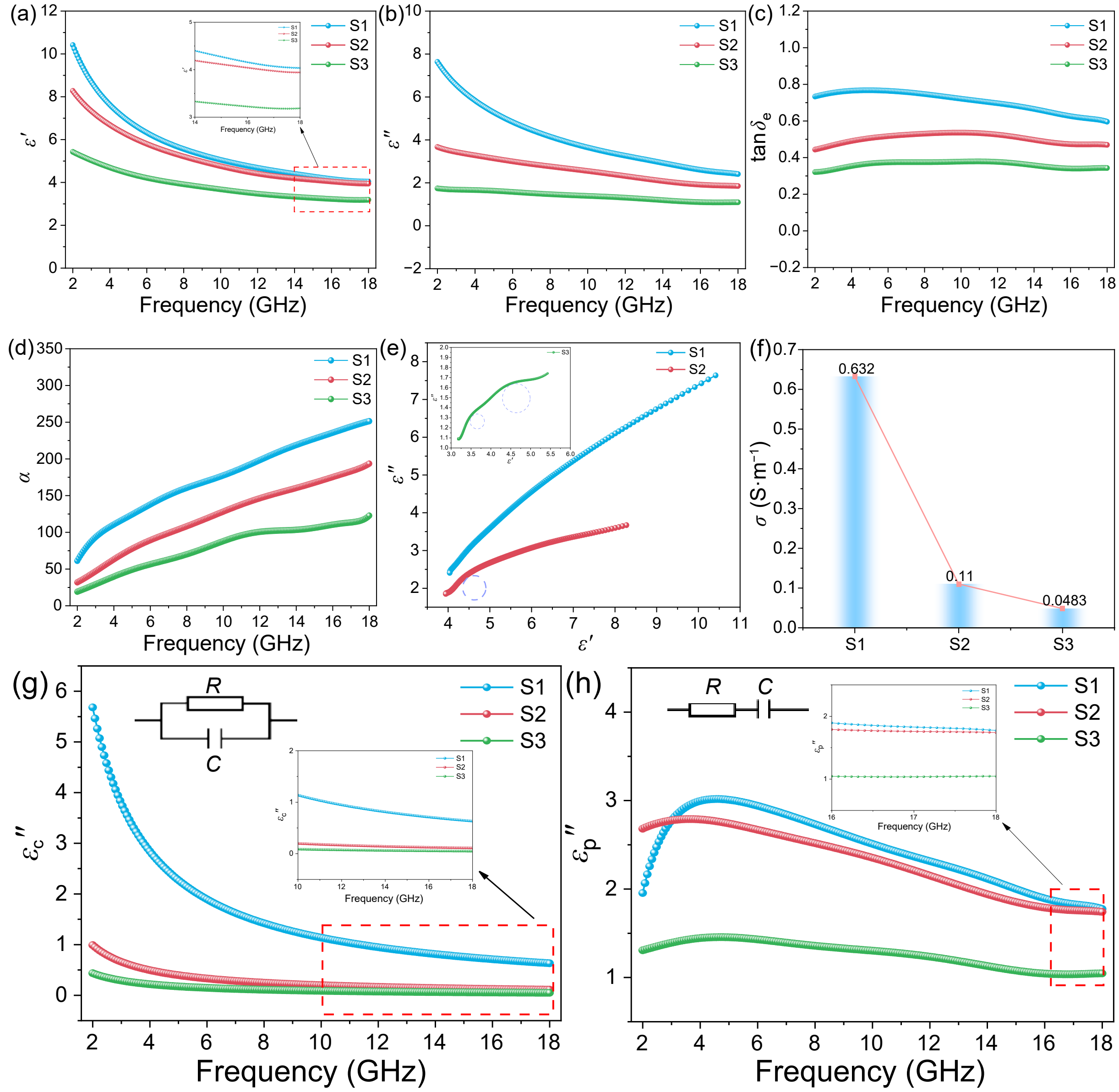

Figure 5 Frequency dependence of (a) ε', (b) ε'', (c) $\tan\delta_e$, and (d) α for S1–S3. (e) Cole–Cole curves and (f) histograms of electrical conductivity of S1–S3. (g) Fitted conduction loss and (h) polarization loss versus frequency plots for S1–S3.

Herein μ_0 represents the vacuum permeability. As shown in Fig. 6(f), in the low-frequency region, S1 exhibits a distinct resonance peak, indicating the presence of natural resonance. Within the high-frequency region, C_0 remains largely unchanged, which is a characteristic suggesting the existence of eddy current loss [43, 44].

Usually, the impedance matching characteristic can be assessed by the modulus of normalized input impedance ($|Z_{in}/Z_0|$), which can be calculated by Eq. (7) [45, 46]

$$\left|\frac{Z_{in}}{Z_0}\right| = \left|\sqrt{\frac{\mu_r}{\varepsilon_r}}\tanh\left[j\left(\frac{2\pi fd}{c}\right)\sqrt{\mu_r\varepsilon_r}\right]\right| \tag{7}$$

Figures 6(g)–6(i) show the contour maps of $|Z_{in}/Z_0|$ for S1–S3. The area enclosed by the blue lines represents the values of $|Z_{in}/Z_0|$ within the range of 0.8 to 1.2, while the red line denotes the situation where $|Z_{in}/Z_0|$ equals 1. Impressively, S2 has the largest enclosed area when $|Z_{in}/Z_0| = 1$, which indicates that it has the optimal impedance matching characteristic. Consequently, S2 demonstrates the best impedance matching and moderate attenuation loss, thus possessing the strongest EMW absorption performance.

Figure 7 shows the possible EMW absorption mechanism of NRGO/$MgFe_2O_4$@NC composite aerogel (S2). Firstly, according to Maxwell–Garnett theory, the effective dielectric constant (ε_{eff}) of porous materials can be expressed as the following equations [25, 28]

$$\varepsilon_{eff}^{MG} = \left[\frac{(\varepsilon_1 + 2\varepsilon_2) + 2v(\varepsilon_1 - \varepsilon_2)}{(\varepsilon_1 + 2\varepsilon_2) - v(\varepsilon_1 - \varepsilon_2)}\right]\varepsilon_2 \tag{8}$$

$$\varepsilon_{eff}^{MG} = \left[1 - \frac{3v(\varepsilon_2 - 1)}{(1 + 2\varepsilon_2) + v(\varepsilon_2 - 1)}\right]\varepsilon_2 \tag{9}$$

where v represents the volume fraction of guest, and ε_1 and ε_2 represent dielectric constants of guest and host, respectively. Generally, the dielectric constant of gaseous state materials is

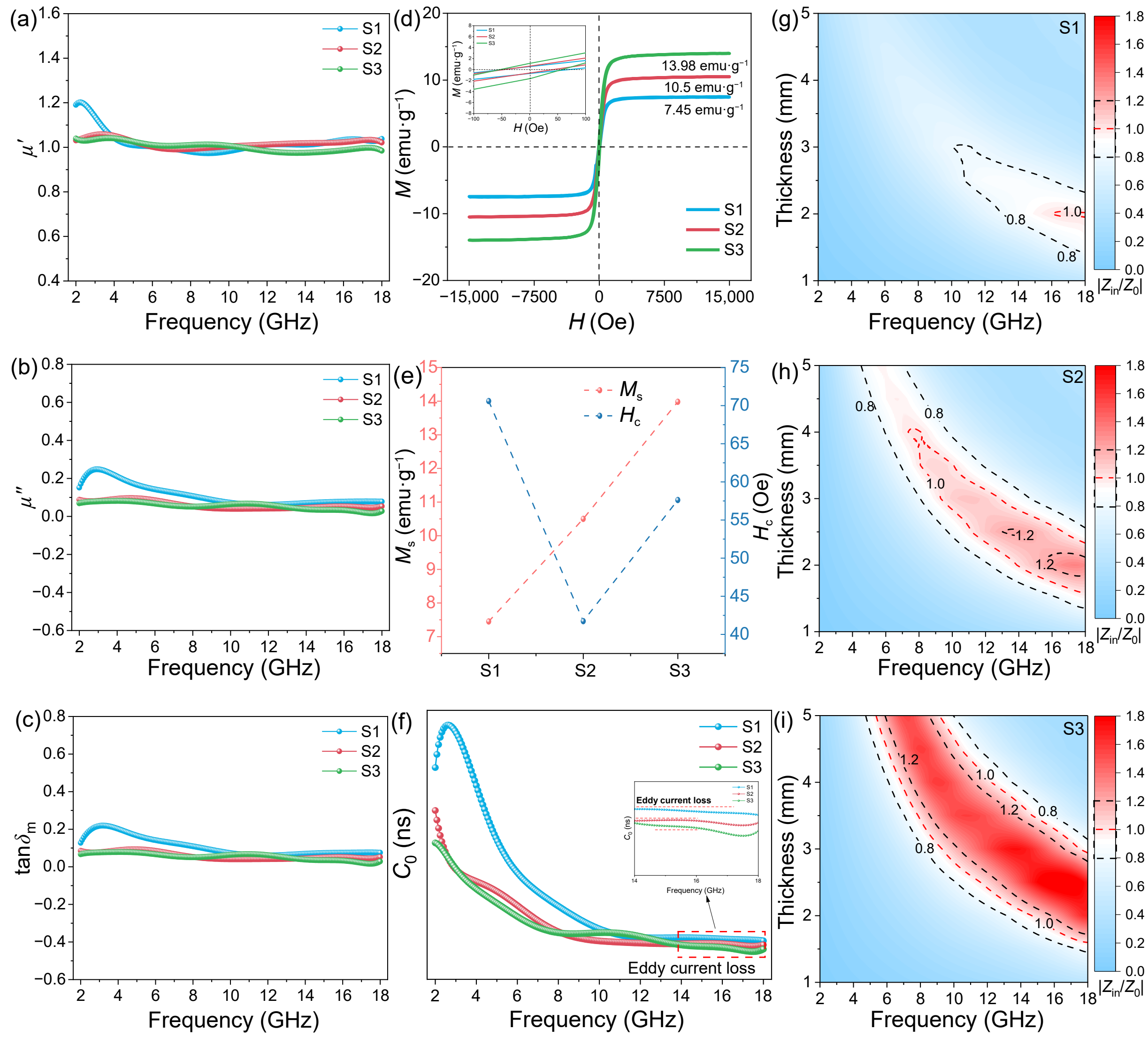

Figure 6 Frequency dependence of (a) μ', (b) μ'', and (c) $\tan\delta_m$. (d) Hysteresis loops at room temperature for S1–S3. (e) M_s and H_c versus sample curves. (f) C_0 versus f curves of S1–S3. Contour maps of $|Z_{in}/Z_0|$ for (g) S1, (h) S2, and (i) S3.

considered as 1, while that of solid materials is larger than 1. Thus, Eq. (8) is reduced to Eq. (9). From Eq. (9), it can be deduced that the volume fraction of air has a modulating effect on the relative permittivity of porous materials [25, 28]. Therefore, the unique porous structure in the NRGO/$MgFe_2O_4$@NC composite aerogel will optimize the impedance matching between the absorber and air by regulating the dielectric constant [25, 28]. Meanwhile, the stacking of neighboring NRGO flakes forms a 3D porous network, which will effectively attenuate the electromagnetic energy through multiple reflections inside the porous aerogel [25, 28]. Secondly, according to Cao's electron hopping model, the electrons can absorb electromagnetic energy and then migrate on the surface of NRGO, thereby generating conduction loss [47, 48]. Thirdly, $MgFe_2O_4$@NC microspheres with the core–shell structure are almost uniformly distributed on the surface of wrinkled NRGO flakes, thus numerous heterogeneous interfaces can be produced between $MgFe_2O_4$ and NC, and NRGO and $MgFe_2O_4$@NC. As a result, the space charges will gather at the heterogeneous interfaces, forming a capacitor-like structure that generates interfacial polarization [25, 28]. Fourthly, the results of Fourier transform infrared (FT-IR), Raman spectra, and XPS spectra show that there are residual oxygen-containing functional groups and structural defects on the surface of NRGO, which can act as the polarization centers, thereby inducing dipole polarization and further attenuating the electromagnetic energy [15, 25, 28]. In addition, the successful doping of N atoms into RGO will disrupt the sp^2 hybridization distribution of C, which in turn leads to the formation of disordered sites and sp^3 defects. Due to the difference in electronegativity between C and N atoms, the resulting C–N dipole can rotate under the action of alternating electromagnetic fields, leading to dipole polarization and thereby more effectively attenuating the energy of the incident waves [28, 29]. Finally, the presence of ferromagnetic $MgFe_2O_4$ endows the magnetic loss of the composite aerogel in the form of eddy current loss, thereby helping to enhance the EMW attenuation capacity.

3.4 Radar cross section (RCS) simulation

To evaluate the radar stealth capacity of NRGO/$MgFe_2O_4$@NC composite aerogels, the RCS results of the coated perfect electrical conductor (PEC) substrate model and all the samples under actual

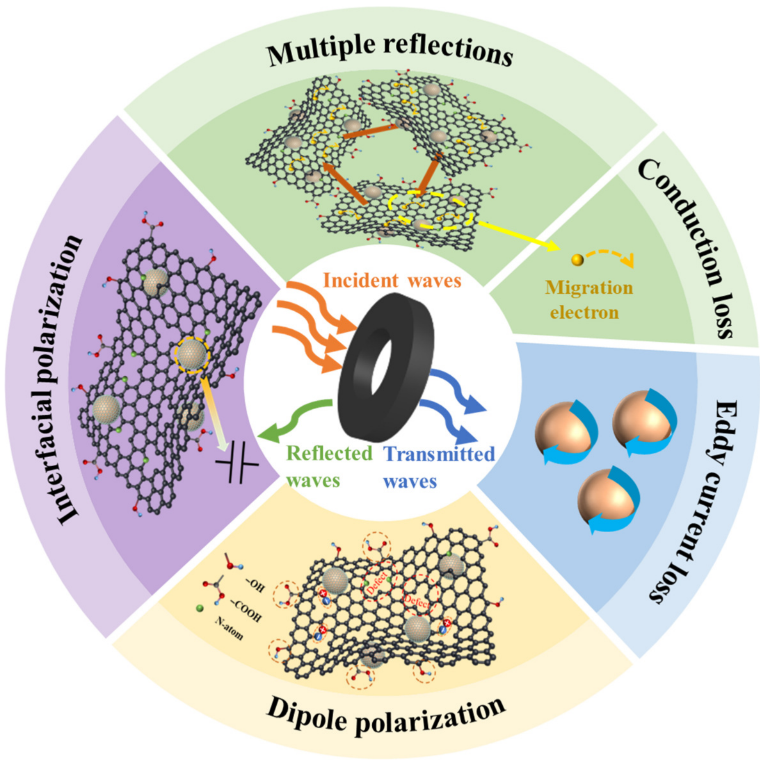

Figure 7 Schematic diagram of the EMW absorption mechanism of NRGO/$MgFe_2O_4$@NC composite aerogel.

far-field conditions (Fig. 8(a)) are simulated by computer simulation technology (CST) software, with the *Z*-axis of the model as the direction of incidence orientation of the waves, and the detection angle is θ [49–51]. The thicknesses of the PEC layer and the absorber layer are 0.5 and 1.97 mm, respectively, and the electromagnetic field frequency is 17.28 GHz. As shown in Fig. 8(b), among the three samples, the RCS value of S2 decreases the most, reaching 36.14 dB·m^2. From Figs. 8(c)–8(f), it can be seen that the PEC model has the strongest plane scattering signal, while the PEC model covered with S2 shows the weakest plane scattering signal, suggesting that S2 possesses the strongest radar wave dissipation capacity [52, 53]. Figures 8(g)–8(j) show the RCS simulation diagrams of the PEC model and the model covered with S1–S3. The minimum RCS values of these models are −17.90, −27.96, −44.93, and −27.42 dB·m^2, respectively. Therefore, the RCS simulation results indicate that S2 has excellent radar stealth capacity.

3.5 Thermal insulation properties

Aerogels with a special 3D porous network structure have been widely applied in the field of thermal management [50–52]. As shown in Fig. 9, the center temperature of the sample is marked as P1, the high-temperature area of the sample platform is labeled as P2, and the room temperature is marked as P3. The infrared thermal camera records the temperature change on the top surface of sample from 1 to 10 min. The results show that the center temperatures of S1 are measured as 33.8, 34.3, 35.7, 36.4, 37.0, 38.1, 38.5, 39.0, 40.1, and 40.1 °C (Fig. S6 in the ESM). Under the same conditions, the center temperatures of S2 are measured as 34.6, 35.2, 35.6, 35.8, 36.1, 36.7, 37.1, 37.5, 38.3, and 38.3 °C (Fig. 9). For S3, the center temperatures are recorded as 34.5, 35.1, 35.8, 36.7, 37.8, 38.1, 38.4, 38.9, 39.6, and 39.6 °C (Fig. S7 in the ESM). After 10 min, the temperatures of all the samples had stabilized without any significant fluctuations. In the thermal imaging images, the distinct color difference between the center of the sample and the high-temperature area indicates that S2 has the best thermal insulation performance.

The thermal conductivity of NRGO/$MgFe_2O_4$@NC composite aerogels was measured using the transient plane source method to evaluate their thermal insulation performance. As shown in Fig. 9(k), the thermal conductivities of all three samples are extremely low (S1: 51 mW·m^{-1}·K^{-1}, and S2: 34 mW·m^{-1}·K^{-1}), confirming their excellent thermal insulation capability. Particularly, S3 has the lowest thermal conductivity of 31 mW·m^{-1}·K^{-1}, which is even lower than that of common commercial insulation materials such as phenolic resin (PF, 32 mW·m^{-1}·K^{-1}) and expanded polystyrene (EPS, 33 mW·m^{-1}·K^{-1}) [54]. The superior thermal insulation properties of these aerogels can be attributed to their unique 3D hierarchical porous structure, which effectively traps stationary air (an excellent thermal insulator) within the interconnected pores. Additionally, the labyrinth-like network formed by the stacking of NRGO flakes and the embedded $MgFe_2O_4$@NC microspheres significantly prolongs the thermal transfer path and enhances phonon scattering, thereby further inhibiting thermal conduction [55]. This integrated design not only ensures extremely low thermal conductivity but also synergistically promotes the overall multifunctionality of the aerogels, making them promising candidates for thermal management applications in harsh environments.

4 Conclusions

In summary, NRGO/$MgFe_2O_4$@NC composite aerogels with low bulk density (9.1–12.3 mg·cm^{-3}) were successfully prepared by solvothermal synthesis, *in-situ* polymerization, annealing treatment, and hydrothermal self-assembly processes. The results of

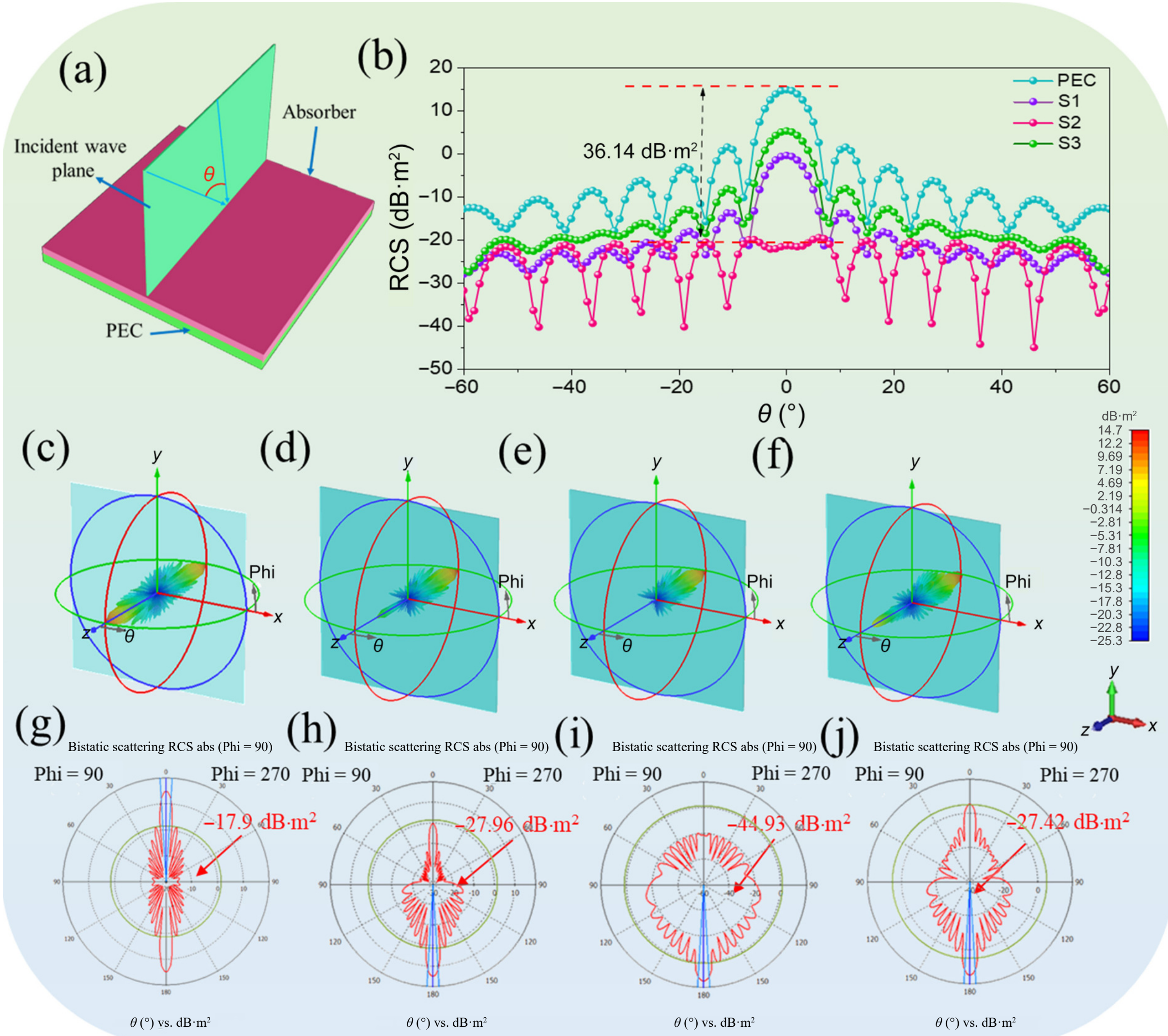

Figure 8 (a) CST simulation model. (b) RCS simulation curves. Far-field simulation results of (c) the PEC model and the models covered with (d) S1, (e) S2, and (f) S3. RCS values of (g) the PEC model and the models covered with (h) S1, (i) S2, and (j) S3.

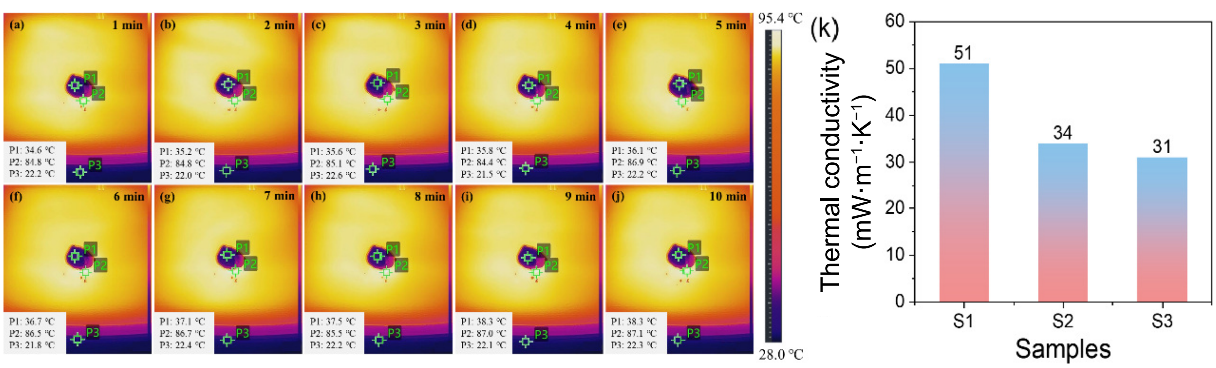

Figure 9 (a)–(j) Infrared thermal imaging images of S2. (k) Histograms of thermal conductivity of S1–S3.

morphological analysis revealed that the ternary composite aerogels had a unique 3D porous network structure, and the $MgFe_2O_4$@NC core–shell microspheres were almost uniformly distributed on the surface of wrinkled NRGO sheets, forming abundant heterogeneous interfaces, thereby significantly improving the EMW absorption performance. Significantly, when the addition amount of $MgFe_2O_4$@NC was 30 mg and φ_w was only 6 wt.%, the optimal RL_{min} of −59.79 dB and the maximum EAB of 7.2 GHz (10.88–18 GHz) were reached. The possible EMW absorption mechanism of NRGO/$MgFe_2O_4$@NC composite aerogels was also proposed, which could be attributed to the optimized impedance matching, synergistic effect of the conduction loss, polarization loss, and eddy current loss, as well as multiple reflections. Additionally, the ternary composite aerogels exhibited excellent radar stealth and thermal insulation properties. Therefore, this study provides new insights into the construction of graphene-based porous composites as multifunctional EMW absorbing materials.

Electronic Supplementary Material: Supplementary material (raw materials, characterization methods, and RCS simulation; physical parameters and FT-IR analysis of S1–S3; SEM images and histograms of the particle size distribution of $MgFe_2O_4$, $MgFe_2O_4$@PDA, and $MgFe_2O_4$@NC; RL–*f* curves with different filling ratios of S2; and thermal imaging images of S2 and S3) is available in the online version of this article at https://doi.org/10.26599/NR.2026.94908344.

Data availability

All data needed to support the conclusions in the paper are presented in the manuscript and the Electronic Supplementary Material. Additional data related to this paper may be requested from the corresponding author upon request.

Acknowledgements

This work was financially supported by the National Natural Science Foundation of China (Nos. 52502056, 52402140, and 51707003), Open Research Fund Program of Engineering Technology Research Center of Coal Resources Comprehensive Utilization, Anhui Province, Anhui University of Science and Technology (No. MTYJZX202301), Joint National-Local Engineering Research Center for Safe and Precise Coal Mining Fund (No. EC2022020), Anhui Provincial Natural Science Foundation (No. 2008085J27), and Research and Development Project of Chengdu Tory Thalez Electronic Application Technology Co., Ltd. (No. HX20240072).

Declaration of competing interest

All the contributing authors report no conflict of interests in this work.

Author contribution statement

R. W. S.: Conceptualization, methodology, validation, writing – original draft, writing – review & editing, funding acquisition, project administration, resources. Y. R. Z.: Data curation, software, investigation. K. L. Y.: Software, investigation. Y. M. L.: Software, investigation. X. Q. Z.: Formal analysis, funding acquisition. B. W.: Formal analysis, funding acquisition. K. H. T.: Methodology, resources. X. L. J.: Formal analysis, funding acquisition. Z. J. Y.: Project administration, resources. All the authors have approved the final manuscript.

Use of AI statement

None.

References

[1] Chen, W.; Duan, Y. P.; Gu, S. D.; Zhang, M.; Xia, C. Y. Resonator-free metamaterials based on ferromagnetic dielectrics for mandatory microwave loss and compact stealth cloaks. *Adv. Mater.* **2025**, *37*, 2507366.

[2] Liu, A.; Xu, X. S.; Qiu, H.; Guo, H.; He, M. K.; Yu, Z.; Zhang, Y. L.; Gu, J. W. Bioinspired hollow heterostructure fillers for enhanced electromagnetic interference shielding in polyimide aerogels. *InfoMat* **2025**, *7*, e70060.

[3] Zhao, J.; He, M. K.; Guo, H.; Zhang, Y. L.; Qiu, H.; Lai, H. R. Multidimensional construction of 1T-MoS_2@graphene nanosheets nanocomposites for enhanced electromagnetic wave absorption. *J. Mater. Sci. Technol.* **2025**, *218*, 35–44.

[4] Jiang, H. T.; Wang, Y. X.; Wang, C. J.; Wang, Y. B.; Sun, Y.; Guo, J. H.; Ding, B. H.; Dai, S. C.; Liu, D. M.; Li, H. Construction of MIL-88C/$CuCo_2S_4$-derived bamboo-like carbon nanotubes/carbon nanofiber aerogels for high-efficiency microwave absorption and thermal insulation performances. *Nano Res.* **2025**, *18*, 94907849.

[5] Guo, Y.; Duan, Y. P.; Liu, X. J.; Tian, J.; Wen, N. X.; Fan, Z.; Pan, L. J. Construction of rGO/MOF-derived CNTs aerogel with multiple losses for multi-functional efficient electromagnetic wave absorber. *Carbon* **2024**, *230*, 119591.

[6] Chen, W.; Liu, Q. Y.; Zhu, X. X.; Fu, M. One-step *in situ* growth of magnesium ferrite nanorods on graphene and their microwave-absorbing properties. *Appl. Organomet. Chem.* **2018**, *32*, e4017.

[7] Nie, L. J.; Wan, Z. L.; Shu, R. W. Synthesis of magnesium ferrite decorated MXene composites with broadband and high-efficiency microwave dissipation performance. *Compos. Sci. Technol.* **2024**, *256*, 110764.

[8] Meng, F. B.; Wang, H. G.; Huang, F.; Guo, Y. F.; Wang, Z. Y.; Hui, D.; Zhou, Z. W. Graphene-based microwave absorbing composites: A review and prospective. *Compos. Part B: Eng.* **2018**, *137*, 260–277.

[9] Li, Y. M.; Yun, K. L.; Yi, X.; Wang, C.; Ding, X.; Kang, S.; Kong, D. H.; Xing, J. Q.; Gao, K. P.; Wang, B. et al. Reduced graphene oxide-based magnetoelectric composites for efficient microwave absorption: State of the art and prospects. *Carbon* **2025**, *244*, 120719.

[10] Wang, C.; Han, X. J.; Xu, P.; Zhang, X. L.; Du, Y. C.; Hu, S. R.; Wang, J. Y.; Wang, X. H. The electromagnetic property of chemically reduced graphene oxide and its application as microwave absorbing material. *Appl. Phys. Lett.* **2011**, *98*, 072906.

[11] Zhang, M. M.; Jiang, Z. Y.; Lv, X. Y.; Zhang, X. F.; Zhang, Y. H.; Zhang, J. W.; Zhang, L.; Gong, C. H. Microwave absorption performance of reduced graphene oxide with negative imaginary permeability. *J. Phys. D: Appl. Phys.* **2019**, *53*, 02LT01.

[12] Lu, Z. L.; Zhao, Z. W.; Gong, W. P.; Zhang, H.; Pang, M. Z.; Tang, X. Z. The impact of reduction mode on the microwave absorption characteristics of reduced graphene oxide aerogels. *J. Alloys Compd.* **2024**, *991*, 174451.

[13] Wang, L. B.; Liu, H.; Lv, X. L.; Cui, G. Z.; Gu, G. X. Facile synthesis 3D porous MXene $Ti_3C_2T_x$@RGO composite aerogel with excellent dielectric loss and electromagnetic wave absorption. *J. Alloys Compd.* **2020**, *828*, 154251.

[14] Cheng, Z.; Wang, R. F.; Cao, Y. S.; Cai, Z. H.; Zhang, Z. W.; Huang, Y. Intelligent off/on switchable microwave absorption performance of reduced graphene oxide/VO_2 composite aerogel. *Adv. Funct. Mater.* **2022**, *32*, 2205160.

[15] Shu, R. W.; Xu, J.; Nie, L. J.; Shi, J. J. Facile construction of three-dimensional porous netlike reduced graphene oxide/zinc oxide composite aerogels as the lightweight, flame retardant, compression resilience and high-performance electromagnetic wave absorbers. *Compos. Part A: Appl. Sci. Manuf.* **2022**, *160*, 107068.

[16] Wu, Y.; Zhao, Y.; Zhou, M.; Tan, S. J.; Peymanfar, R.; Aslibeiki, B.; Ji, G. B. Ultrabroad microwave absorption ability and infrared stealth property of nano-micro CuS@rGO lightweight aerogels. *Nano-Micro Lett.* **2022**, *14*, 171.

[17] Li, Q. Y.; Liu, L. Y.; Kimura, H.; Fallatah, A. M.; Qiu, H.; Mersal, G. A. M.; Ren, R. N.; Almalki, A. S.; Wu, N. N.; Sun, X. Q. et al. Interfacical polarization dominant rGO aerogel decorated with molybdenum sulfide towards lightweight and high-performance electromagnetic wave absorber. *Carbon* **2025**, *231*, 119738.

[18] Cao, K. Y.; Ye, W. P.; Fang, Y.; Zhang, Y.; Zhao, R.; Xue, W. D.

Construction of three-dimensional porous network Fe-rGO aerogels with monocrystal magnetic Fe_3O_4@C core-shell structure nanospheres for enhanced microwave absorption. *Mater. Today Phys.* **2024**, *42*, 101383.

[19] Zhao, H. B.; Cheng, J. B.; Zhu, J. Y.; Wang, Y. Z. Ultralight CoNi/rGO aerogels toward excellent microwave absorption at ultrathin thickness. *J. Mater. Chem. C* **2019**, *7*, 441–448.

[20] Qiu, J. F.; Cao, H. P.; Liao, J.; Du, R. X.; Dou, K.; Tsidaeva, N.; Wang, W. 3D porous coral-like $Co_{1.29}Ni_{1.71}O_4$ microspheres embedded into reduced graphene oxide aerogels with lightweight and broadband microwave absorption. *J. Colloid Interface Sci*. **2022**, *609*, 12–22.

[21] Zhao, H.; Gao, H. F.; Jin, S. L.; Yao, Y. X.; Li, X.; Zhang, J. J.; Zong, Q.; Ren, L. L. Exploring interfacial engineering in 3D porous, lightweight $ZnFe_2O_4$/rGO aerogel for electromagnetic wave absorption. *J. Alloys Compd.* **2023**, *957*, 170326.

[22] Lei, D. Y.; Liu, C. K.; Dong, C. L.; Wang, S. J.; Zhang, P.; Li, Y.; Liu, J. X.; Dong, Y. L.; Zhou, C. X. Reduced graphene oxide/MXene/FeCoC nanocomposite aerogels derived from metal-organic frameworks toward efficient microwave absorption. *ACS Appl. Nano Mater.* **2024**, *7*, 230–242.

[23] Shu, Y.; Zhao, T. K.; Abdul, J.; Li, X. H.; Yang, L.; Luo, F. High-efficient electromagnetic wave absorption of coral-like Co/CoO/RGO hybrid aerogels with good hydrophobic and thermal insulation properties. *Chem. Eng. J.* **2023**, *471*, 144535.

[24] Zhou, J.; Chen, Y. J.; Li, H.; Dugnani, R.; Du, Q.; UrRehman, H.; Kang, H. M.; Liu, H. Z. Facile synthesis of three-dimensional lightweight nitrogen-doped graphene aerogel with excellent electromagnetic wave absorption properties. *J. Mater. Sci.* **2018**, *53*, 4067–4077.

[25] Shu, R. W.; Zhang, G. Y.; Zhang, C.; Wu, Y.; Zhang, J. B. Nitrogen-doping-regulated electromagnetic wave absorption properties of ultralight three-dimensional porous reduced graphene oxide aerogels. *Adv. Electron. Mater.* **2021**, *7*, 2001001.

[26] Huang, X. G.; Zhang, L.; Yu, G. Y.; Wei, J. W.; Shao, G. F. Polarization genes dominated heteroatom-doped graphene aerogels toward super-efficiency microwave absorption. *J. Mater. Chem. C* **2023**, *11*, 9804–9814.

[27] Tan, L. L.; Chen, X.; Han, R. H.; Wu, X. Z.; Yang, S. R.; Huang, J. X. Multi-scale doping-Induced impedance matching of graphene aerogel enables ultra-broadband microwave absorption. *Chem. Eng. J.* **2025**, *504*, 158947.

[28] Shu, R. W.; Nie, L. J.; Zhao, Z. W.; Yang, X. H. Synthesis of nitrogen-doped reduced graphene oxide/magnesium ferrite/ polyaniline composite aerogel as a lightweight, broadband and efficient microwave absorber. *J. Mater. Sci. Technol.* **2024**, *175*, 115–124.

[29] Tang, J. M.; Liang, N.; Wang, L.; Li, J.; Tian, G.; Zhang, D.; Feng, S. H.; Yue, H. J. Three-dimensional nitrogen-doped reduced graphene oxide aerogel decorated with Ni nanoparticles with tunable and unique microwave absorption. *Carbon* **2019**, *152*, 575–586.

[30] Yang, Y. W.; Yang, X.; Zhang, Y.; Ye, W. P.; Cao, K. Y.; Zhao, R.; Zheng, T.; Wang, W. J.; Xue, W. D. Three birds with one stone: PDA protection strategy efficiently enhance electromagnetic wave absorption performance. *Carbon* **2025**, *243*, 120528.

[31] Huang, M. Q.; Wang, L.; Pei, K.; Li, B. X.; You, W. B.; Yang, L. T.; Zhou, G.; Zhang, J. C.; Liang, C. Y.; Che, R. C. Heterogeneous interface engineering of Bi-metal MOFs-derived $ZnFe_2O_4$-ZnO-Fe@C microspheres via confined growth strategy toward superior electromagnetic wave absorption. *Adv. Funct. Mater.* **2024**, *34*, 2308898.

[32] Shao, G. F.; Guo, L. Q.; Xu, R. P.; Wu, Y. F.; Huang, X. G. Carbon nanofiber aerogel microspheres with heterogeneous skin–core structure for broadband electromagnetic wave absorption. *Carbon* **2024**, *228*, 119416.

[33] Pan, F.; Pei, K.; Chen, G.; Guo, H. T.; Jiang, H. J.; Che, R. C.; Lu, W. Integrated electromagnetic device with on–off heterointerface for intelligent switching between wave-absorption and wave-transmission. *Adv. Funct. Mater.* **2023**, *33*, 2306599.

[34] Han, Y. X.; Guo, H.; Qiu, H.; Hu, J. W.; He, M. K.; Shi, X. T.; Zhang, Y. L.; Kong, J.; Gu, J. W. Multimechanism decoupling for low-frequency microwave absorption hierarchical Fe-doped Co magnetic microchains. *Adv. Funct. Mater.* **2025**, *35*, 2506803.

[35] He, M. K.; Zhang, K. Y.; Qiu, H.; Guo, H.; Li, X. C.; Guo, Y. Q.; Zhang, Y. L.; Gu, J. W. Low-frequency microwave absorption composites. *Adv. Sci.* **2025**, *12*, e11580.

[36] Qi, J. M.; Liang, C. B.; Ruan, K. P.; Li, M. K.; Guo, H.; He, M. K.; Qiu, H.; Guo, Y. Q.; Gu, J. W. Cactus-like architecture for synergistic microwave absorption and thermal management. *Natl. Sci. Rev.* **2025**, *12*, nwaf394.

[37] Zhang, R. N.; Yuan, B.; Pan, F.; Liang, H. S.; Jiang, H. J.; Guo, H. T.; Rao, Y. C.; Zheng, S. H.; Ruan, L. Y.; Wu, C. S. et al. Ultratransparent, stretchable, and durable electromagnetic wave absorbers. *Matter* **2025**, *8*, 101956.

[38] Li, T. S.; Qiao, M. K.; Chen, F.; Li, X. C. Electrostatic self-assembled CS/$Ti_3C_2T_x$/Co@CNT composites with gradient carbon structure and wideband microwave absorption. *Nano Res.* **2025**, *18*, 94907696.

[39] Liu, C. Y.; He, T. A.; Hu, C. C.; Qian, Q.; Hao, Y. L.; Xu, L.; Lu, H. Y.; Ji, G. B. The optimized design of sandwich structured SiO_2/C@SiC/SiO_2 composites through numerical simulation for temperature-resistant radar and infrared compatible stealth. *Adv. Funct. Mater.* **2025**, *35*, 2416108.

[40] Yang, Z. Q.; Liang, Q. Q.; Qi, X. S.; Zhan, B. B.; Gong, X.; Qu, Y. P.; Ding, J. F.; Yang, J. L.; Chen, Y. L.; Peng, Q. et al. Hollow engineering in CoNi@air@C@MoS_2 multicomponent composites derived from bimetallic CoNi Prussian blue analogs for ultra-wide bandwidth and strong electromagnetic wave absorption. *J. Mater. Sci. Technol.* **2025**, *212*, 35–43.

[41] Meng, X. W.; Qiao, J.; Liu, J. R.; Wu, L. L.; Wang, Z.; Wang, F. L. Core–shell nanofibers/polyurethane composites obtained through electrospinning for ultra-broadband electromagnetic wave absorption. *Adv. Compos. Hybrid Mater.* **2024**, *7*, 149.

[42] Rao, L. J.; Liu, Z. W.; Wang, L.; You, W. B.; Yang, C. D.; Zhang, R. X.; Xiong, X. H.; Yang, L. T.; Zhang, H. B.; Zhang, J. C. et al. Dimensional engineering of hierarchical nanopagodas for customizing cross-scale magnetic coupling networks to enhance electromagnetic wave absorption. *Adv. Funct. Mater.* **2023**, *33*, 2306984.

[43] Sun, R.; Lv, H. W.; Lian, G. J.; Wang, L.; Huang, M. Q.; You, W. B.; Che, R. C. Dielectric shell regulation in synergy FeCoNi@$ZnIn_2S_4$ microspheres with broadband electromagnetic wave absorption. *Soft Sci.* **2025**, *5*, 35.

[44] Yan, S. Y.; Shao, S. P.; Tang, Y. X.; Zhang, X.; Guo, C.; Wang, L. X.; Liu, J. R.; Wu, L. L.; Wang, F. L. Ultralight hierarchical Fe_3O_4/MoS_2/rGO/$Ti_3C_2T_x$ MXene composite aerogels for high-efficiency electromagnetic wave absorption. *ACS Appl. Mater. Interfaces* **2024**, *16*, 36962–36972.

[45] Zhao, J.; Lai, H. R.; Li, M. Anchoring 1T-MoS_2 petals on N-doped reduced graphene oxide for exceptional electromagnetic wave absorption. *Int. J. Miner. Metall. Mater.* **2025**, *32*, 619–630.

[46] Guo, Y. Q.; Li, P.; Zhao, R. L.; Gu, J. W. Preparation and mechanism of thermally conductive polyimide phase change composites with electromagnetic wave-absorbing performance. *Acta Polym. Sin.* **2025**, *56*, 2347–2360.

[47] Song, W. L.; Cao, M. S.; Hou, Z. L.; Fang, X. Y.; Shi, X. L.; Yuan, J. High dielectric loss and its monotonic dependence of conducting-dominated multiwalled carbon nanotubes/silica nanocomposite on temperature ranging from 373 to 873 K in X-band. *Appl. Phys. Lett.* **2009**, *94*, 233110.

[48] Cao, M. S.; Song, W. L.; Hou, Z. L.; Wen, B.; Yuan, J. The effects of temperature and frequency on the dielectric properties, electromagnetic interference shielding and microwave-absorption of short carbon fiber/silica composites. *Carbon* **2010**, *48*, 788–796.

[49] Liu, Z. L.; Wang, L. H.; Zhao, Y. M.; Ren, J. X.; Wang, H. J.; Hu, J. Q.; Guan, H. T. Environmental adaptability and efficient electromagnetic wave protection of C/Co aerogels by anchoring Co to biomass carbon via the high-temperature induced morphological transformation of ZIF-67. *Nano Res.* **2025**, *18*, 94907581.
[50] Zhou, H. W.; Lin, Y.; Ma, Y. Z.; Han, L. Y.; Cai, Z. X.; Cheng, Y.; Yuan, Q. B.; Huang, W. H.; Yang, H. B.; Che, R. C. Hierarchical structure Fe@CNFs@Co/C elastic aerogels with intelligent electromagnetic wave absorption. *InfoMat* **2025**, *7*, e12630.
[51] Guo, Y.; Duan, Y. P.; Gu, S. D.; Liu, X. J.; Fan, Z.; Pang, H. F.; Pan, L. J. Carbon nanocoils-assisted formation of tunable pore graphene aerogels for lightweight broadband microwave absorption, thermal insulation, and antifreeze devices. *Small* **2025**, *21*, 2412270.
[52] Shao, S. P.; Xing, S. Z.; Bi, K.; Zhao, T. T.; Wang, H.; Tang, Y. X.; Liu, J. R.; Wang, F. L. Fabrication of graphene/polyimide/Co-N-C aerogel with reinforced electromagnetic losses and broadband absorption for highly efficient microwave absorption and thermal insulation. *Chem. Eng. J.* **2024**, *494*, 152976.
[53] Liu, X. J.; Duan, Y. P.; Wu, N.; Li, G. M.; Guo, Y.; Liu, J. Y.; Zhu, N.; Wang, Q.; Wang, L.; Xu, Z. C. et al. Modulating electromagnetic genes through Bi-phase high-entropy engineering toward temperature-stable ultra-broadband megahertz electromagnetic wave absorption. *Nano-Micro Lett.* **2025**, *17*, 164.
[54] Zhang, X.; Xing, S. Z.; Shao, S. P.; Tang, Y. X.; Wang, Z.; Zhang, Q.; Liu, J. R.; Wang, F. L. Rational micro/nano-architecture design of Fe_3O_4@TiO_2/PI/rGO aerogels for integrated broadband microwave absorption, flame retardancy, and moisture resistance. *Carbon* **2025**, *245*, 120840.
[55] Guo, C.; Shao, S. P.; Zhang, X.; Tang, Y. X.; Wang, L. X.; Liu, J. R.; Wu, L. L.; Bi, K.; Wang, F. L. Multifunctional MXene/rGO aerogels loaded with Co/MnO nanocomposites for enhanced electromagnetic wave absorption, thermal insulation and pressure sensing. *Nano Res.* **2024**, *17*, 7803–7813.